Check for updates

Insights into the role of the covalent Ni–O bonds in LiNiO₂ positive electrodes: a correlative hard X-ray spectroscopy study†

Jazer Jose H. Togonon, ‡[abc] Jean-Noël Chotard, [cde] Alessandro Longo, [fg] Lorenzo Stievano, [ceh] Laurence Croguennec *[bce] and Antonella Iadecola *[ei]

The interest in Ni-rich layered oxide positive electrode materials has been increasing due to their wide applicability particularly in electric vehicles as high capacity and high energy density electrode materials. However, the Ni–O bond array which builds the overall framework and plays a critical role in the charge compensation mechanism of the material requires deeper understanding. This work presents a correlative approach elucidating the role of the local highly covalent Ni–O bonds in a LiNiO₂ (LNO) model material. Pristine and electrochemically obtained LNO positive electrodes are analyzed using *ex situ* X-ray diffraction (XRD) and extended X-ray absorption fine structure (EXAFS) to compare the average and local structural evolution upon Li⁺ ion de-intercalation. Insights from Ni K-edge X-ray absorption near-edge structure (XANES) and non-resonant Ni Kβ X-ray emission spectroscopy (XES) spectra are combined to track the electronic environment of Ni. X-ray Raman scattering (XRS) spectra at the Ni L₂,₃-edges and O K-edge provide direct bulk electronic information with regard to the interplay between Ni 3d and O 2p states. The overall findings imply that O plays a significant role in the charge compensation process, contributing to the substantial negative charge transfer from the O 2p orbitals, because of the covalency in the Ni–O bonds inside the NiO₂ framework within the edge-sharing NiO₆ octahedra. The utilization of complementary X-ray spectroscopy techniques clarifies the intricate electronic environment of LNO, which is helpful in understanding Ni-rich positive electrode materials and offering new insights into their covalent nature.

[a]Synchrotron SOLEIL, L'Orme des Merisiers, Saint-Aubin, 91192 Gif-sur-Yvette, France

[b]Univ. Bordeaux, CNRS, Bordeaux INP, ICMCB, UMR 5026, F-33600 Pessac, France. E-mail: laurence.croguennec@icmcb.cnrs.fr

[c]ALISTORE-ERI European Research Institute, FR CNRS 3104, F-80039 Amiens Cedex 1, France

[d]Université de Picardie Jules Verne, Laboratoire de Réactivité et Chimie des Solides (LRCS), 15 Rue Baudelocque, Amiens, 80000, France

[e]RS2E, Réseau Français sur le Stockage Electrochimique de l'Energie, FR CNRS 3459, Amiens F-80039 Cedex 1, France. E-mail: antonella.iadecola@synchrotron-soleil.fr

[f]European Synchrotron Radiation Facility (ESRF), 71, Avenue des Martyrs, Grenoble F-38000, France

[g]Istituto per lo Studio dei Materiali Nanostrutturati (ISMN)-CNR, UOS Palermo, Via Ugo La Malfa 153, Palermo 90146, Italy

[h]ICGM, Univ. Montpellier, CNRS, ENSCM, 34095 Montpellier, France

[i]Sorbonne Université, CNRS, Physicochimie des Électrolytes et Nanosystèmes Interfaciaux, F-75005 Paris, France

† Electronic supplementary information (ESI) available. See DOI: https://doi.org/10.1039/d5ta03573b

‡ Present address: Université Grenoble Alpes, CEA, CNRS, Grenoble INP, IRIG, SyMMES, 38000 Grenoble, France.

1 Introduction

The design of positive electrode materials for lithium-ion batteries has been driven towards the goal of having enhanced safety and achieving high-energy density. For instance, transition metal (TM) layered oxide positive electrode materials, such as NMC (LiNi₁₋ₓ₋ᵧMnₓCoᵧO₂) and NCA (LiNi₁₋ₓ₋ᵧCoₓAlᵧO₂), $x \geq 0.8$, have been suitably formulated in line with specific target applications.[1–3] In these compounds, nickel allows for high capacity and energy density, while aluminum or manganese improves thermal stability, and cobalt stabilizes the layered structure, further enhancing cyclability.[4–6] As a need arises to obtain higher capacity and energy density, Ni-rich NMC and NCA compounds primarily depend on the nickel content in the material. However, increasing the energy density often entails expanding the voltage windows to fully extract Li⁺ ions, which can lead to several detrimental issues, including bulk structural and surface phase transformations, and eventually gas release.[7–9] To mitigate these issues, it is essential to fundamentally understand the electronic environment of the local Ni–O bond and its role in the charge compensation process, which is still a subject of significant debate in Ni-rich layered oxides (Fig. 1).

Towards this goal, the interest in LiNiO₂ (LNO) has been renewed. The understanding of the atomic and electronic structure of pristine LNO, as well as the charge compensation mechanism during Li⁺ ion extraction, remains contentious. The
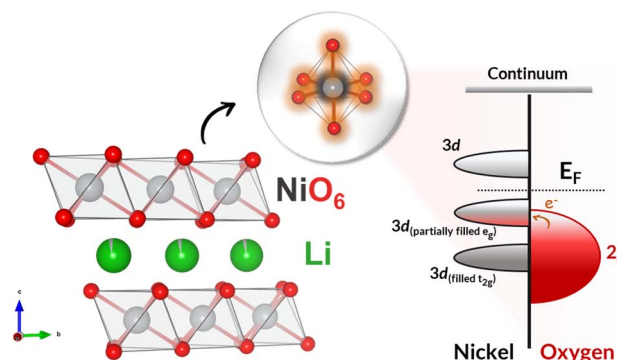
Fig. 1 Representative NiO_2 layers made of edge-sharing NiO_6 octahedra and a Li interlayer from the crystal structure of $LiNiO_2$, highlighting a local NiO_6 unit. A simplified band structure model of the Ni and O states is presented.

charge balance arguments of LNO suggest an ionic distribution of Li^+, Ni^{3+}, and O^{2-} ions. However, regardless of the synthesis conditions and methods, LNO tends to contain an excess of Ni^{2+} ($2z$), resulting in the general formula $Li_{1-z}Ni_{1+z}O_2$ where z represents the fraction of nickel occupying the lithium layer in the structure.[10–13] This implies an average oxidation state of Ni equivalent to $(3 + z)/(1 + z)$, corresponding to the zNi^{2+} counterparts that are created in the Ni slab.[10,14] Consequently, this affects the Li–O and especially the Ni–O distances in the average structure. Meanwhile, the local atomic environment around Ni in LNO has its own peculiarity. Earlier theoretical studies suggested that LNO could exhibit both bond disproportionation (BD) due to mixed valence states of Ni^{2+} and Ni^{3+} and Jahn–Teller (JT) distortion in the Ni^{3+} system.[15] More recent computational studies propose that the ground state of LNO may be a high-entropy, bond-disproportionated glass, with JT distortion dynamically reorienting on the picosecond timescale.[16,17] A static random orientation of JT distortion was also proposed based on neutron pair distribution function analysis,[18] while an extended X-ray absorption fine structure (EXAFS) study revealed a non-cooperative JT effect in the local distortion of NiO_6 octahedra.[19] These hypotheses entail that varying electronic configurations of Ni exist, mainly depending on the Ni–O bond framework.

Since the charge compensation mechanism upon Li^+ ion deintercalation depends on the oxidation state of Ni in LNO, it is crucial to establish the starting point for the Ni content (i.e., the value of z) and the corresponding average Ni oxidation state in the studied LNO sample while the target here is analyzing the overall structural and electronic changes (Fig. 1). During delithiation, Ni^{3+} is expected to be oxidized to Ni^{4+}, both in their ionic low-spin configurations of $t_{2g}^6 e_g^1$ to $t_{2g}^6 e_g^0$. Moreover, it is important to note that high-voltage cycling is often attributed not only to the activation of the Ni^{4+}/Ni^{3+} redox couple, but also to the involvement of the O^{2-}/O^{n-} anionic redox process.[20] Some studies indicate an increase in Ni–O bond covalency, with electron–hole density shifting towards oxygen when nickel is highly oxidized as there exists a strong Ni 3d–O 2p orbital

overlap.[16,21,22] Others propose that dimerization of O occurs and is triggered similarly to that in Li-rich systems.[23,24]

Various spectroscopic techniques, such as Ni K-edge X-ray absorption near edge structure (XANES)[25,26] and soft X-ray absorption spectroscopy (soft-XAS),[23,27–30] at both Ni $L_{2,3}$- and O K-edges have been used to probe the charge compensation mechanism, revealing the involvement of nickel and probing the participation of oxygen. However, in the case of soft-XAS, the probing depth is limited to 5–100 nm depending on the detection mode, either electron yield or fluorescence yield, the former being mostly reported.[20,27] More recently, hard X-ray photoelectron spectroscopy (HAXPES) was used to probe the role of oxygen in the bulk charge compensation mechanism.[31] In addition to these techniques, resonant inelastic X-ray scattering (RIXS) spectroscopy was also explored to directly probe the involvement of O^{2-}.[20,32] Yet, limitations such as spectral overlap, low cross-section for specific oxygen-related transitions, and sensitivity to experimental conditions together with beam-induced surface artefacts[33] have constrained its ability to provide definitive insights into the role of oxygen in redox processes. Despite these characterization tools, the lack of a comprehensive understanding of the bulk electronic structure of the material has been a major challenge in this field. Therefore, a detailed description of both the long-range and local structure, along with the electronic environment, needs to be achieved using complementary techniques on standardized samples to eliminate biases originating from the sample preparation. Moreover, the sequential evolution of such environments upon the electrochemical deintercalation of Li^+ ions is still underexplored.

X-ray Raman Scattering (XRS) is a suitable tool for accessing soft X-ray edges using a hard X-ray photon. In particular, it is possible to measure the O K-edge and the Ni $L_{2,3}$-edges, thus providing bulk information (>10 μm) on charge compensation mechanisms while overcoming the limitations of soft X-ray measurements.[34,35] In fact, in the low-q geometrical configuration, the XRS spectra are consistent with those of soft-XAS, but with significantly less stringent experimental requirements. Unlike soft-XAS, XRS does not require an ultra-high vacuum sample environment, enabling operando measurements to be conveniently performed in a conventional electrochemical cell.[36–39] In addition, non-resonant X-ray emission spectroscopy (XES), which is almost simultaneously measured with XRS, at the Ni core-to-core (CtC) and valence-to-core (VtC) Kβ emission lines can complement Ni K-edge XAS in the understanding of the Ni electronic environment, as it probes electronic transitions of occupied states close to the Fermi level, which is expected to be sensitive to valence states.[40–42]

In this study, pristine LNO and electrochemically delithiated samples at different states of charge, corresponding to various Li contents, are characterized using ex situ XRD and complementary hard X-ray spectroscopic techniques, including XAS, XES, and XRS. This approach provides a comprehensive and holistic view of the long-range average structure and the local structure, as well as the electronic environment of Ni and O in the materials, offering a direct probe to the nature of Ni–O bonds. The same samples are analyzed using different

techniques, eliminating potential biases in the electrochemical preparation of the samples, thereby ensuring the reliability of the results. The study also aims to provide new insights into the covalent Ni–O bonds, which are directly tied to the charge compensation mechanisms in conventional stoichiometric layered oxide positive electrodes, particularly at high states of charge.

2 Materials and methods

2.1 Electrochemical cycling and sample preparation

Tape-cast LNO positive electrodes (94 : 3 : 3 ratio of LNO, carbon black, and PVDF (BASF)) with a diameter of 14 mm were assembled in conventional 2325-coin cells in a half-cell configuration with a stack consisting of a Li metal acting as the negative and counter electrode and Whatman glass fiber as the separator. Commercial LP30 (Solvionic, >99.9%), consisting of 1 M $LiPF_6$ dissolved in a 1 : 1 v/v mixture of ethylene carbonate (EC) and dimethyl carbonate (DMC), was used as the electrolyte.

The cells were cycled at a constant current of 0.0641 mA, equivalent to a C/24 rate (where 1C corresponds to a complete charge in 1 hour), relative to an areal capacity of 1 mAh cm^{-2}. Charging was stopped when the target voltage, corresponding to the deintercalation of the desired amount of Li^+ ions, was reached. The cut-off voltage and the Li content were chosen based on the expected crystallographic phase transformations demonstrated for LNO during cycling (i.e., at C/24, at 3.72 V, 3.86 V, 4.04 V, 4.13 V and 4.30 V vs. Li^+/Li). When the target voltage is reached, the cells are stopped and immediately dismantled in an Ar-filled glovebox to reduce relaxation times and to preserve their state of charge and structure (complete dismantling within less than 20 min). The recovered electrodes were washed with DMC to remove the excess of electrolyte, dried and stored in a glove box. These electrodes were then divided into four parts to have a uniform sample set for all applied characterization studies. The samples are then sealed in either glass capillaries (for X-ray diffraction measurements) or Kapton films with external plastic protection (for X-ray spectroscopy measurements) to avoid air exposure during the measurements. Individual electrochemical charge profiles obtained at different cut-off voltages labelled X0 to X5 are presented in Fig. S1.†

2.2 X-ray diffraction (XRD) measurements and structural analysis (Rietveld refinement)

Ex situ XRD patterns of pristine and cycled LNO electrodes were collected with a step size of 0.016° using a laboratory PANalytical X'Pert3 diffractometer equipped with a capillary spinner and a Cu $K\alpha_{1,2}$ X-ray source. All measurements were done at room temperature (~25 °C). The powders of pristine and cycled LNO electrodes were recovered by scraping off enough material from the current collector to pack a 0.30 mm diameter glass capillary.

Structural data were derived from Rietveld refinements of the XRD patterns of the pristine and cycled LNO samples using the FullProf Suite software (ESI Note 1†).[43] Detailed

crystallographic information for the pristine material and its electrochemically delithiated phases is given in Tables S1.0–S1.5† (corresponding to X0 to X5, respectively). The obtained cell parameters and the weight composition of the crystalline phases in each sample are presented in Fig. S2.†

2.3 Transmission X-ray absorption spectroscopy (XAS)

Transmission Ni K-edge (8333 eV) XAS measurements were carried out at room temperature at the ROCK beamline of Synchrotron SOLEIL (Saint-Aubin, France).[44] Ni foil was used as a reference for energy calibration. The Si(111) quick-XAS monochromator oscillated at a frequency of 2 Hz. A total of 1200 spectra were averaged over 10 minutes for each sample. The X-ray absorption near edge structure (XANES) and extended X-ray absorption fine structure (EXAFS) data collected for each sample were processed using the DEMETER software package.[45]

EXAFS oscillations were k^2-weighted, and a sine window ($dk = 0$) was applied from 2.65 to 17.5 $Å^{-1}$ for the forward Fourier transform. Fitting was performed in the R range from 1 to 3 Å with a sine window ($dR = 0$) as well for the backward Fourier transform (Fig. S3†). The EXAFS parameter S_0^2 was set to 0.8, and E_0 was defined by the edge position at an absorbance of 0.7 as already reported in a similar XAS study.[26]

2.4 X-ray emission spectroscopy (XES) and X-ray Raman scattering (XRS)

XES and XRS measurements were carried out at room temperature at the ID20 beamline of the European Synchrotron Radiation Facility (Grenoble, France) with a 16-bunch filling mode. The pink beam from four U26 undulators was monochromatized to an incident energy of 9.7 keV using a cryogenically cooled Si(111) monochromator and focused to a spot size of approximately 30 μm × 30 μm ($V \times H$) at the sample position using a mirror system in Kirkpatrick–Baez geometry. The sample was positioned to achieve a 10° grazing incident angle. All XES and XRS measurements were conducted at room temperature using a custom sample holder with an aluminum dome to protect the sample from ambient air. The sample was mounted in the sample holder inside an atmosphere-controlled glovebox to avoid air exposure. Nitrogen gas flow was also introduced into the holder to further prevent air contamination. Beam attenuation was set to 10%. For XES measurements, all Kβ emission lines were collected, covering both the core-to-core (CtC) Kβ region (8110–8300 eV) and the valence-to-core (VtC) Kβ region (8300–8350 eV). Data were collected using an energy-dispersive von Hamos spectrometer equipped with three cylindrically bent Si(440) crystal analyzers with a bending radius of $R = 250$ mm and an incident energy of 9.7 keV.[46] The total integration time for each scan was approximately 15 minutes, and the data were recorded simultaneously using three different detectors. Individual scans were averaged using the PyMCA software package.[47] All spectra were background-subtracted and normalized with respect to the integrated sum of the full range of the Kβ XES. A spline-type baseline for the Kβ VtC region was created using the same approach described in a previous work.[48] In short, the baseline was established using the high-

energy tail of the Ni Kβ CtC emission line (8250–8300 eV) up to the high-energy end of the Kβ VtC region.

The large solid angle spectrometer at ID20 was used to collect XRS data with 36 spherically bent Si(660) crystal analyzers. Full range scans for the O K-edge were measured from 520 to 565 eV with a step size of 0.2 eV by scanning the incident beam energy to record the energy loss. The full range was divided into three regions for scanning: 520–524.8, 525–549.8 and 550–565 eV, with average acquisition times of 3.2, 37.2, and 18.75 minutes, respectively. The Ni $L_{2,3}$ edges were measured from 845 eV to 880 eV with the same step size and a total acquisition time of 43.75 minutes. Repeat scans were performed for all edges, with an average of 6–8 hours per sample, and in different zones to ensure data consistency and to avoid beam damage. All scans were checked for consistency before averaging. The data were processed using the XRStools program package as described elsewhere.[34]

3 Results and discussion

3.1 The average crystal structure and transition metal local environment

The first charge of LNO *vs.* Li metal at C/24 is shown in Fig. 2a, highlighting different states of charge with the expected compositions. The charge profile exhibits several plateaus, characteristic of stoichiometric $LiNiO_2$ (*i.e.*, z close to 0 in $Li_{1-z}Ni_{1+z}O_2$), which represent successive phase transitions

associated with alkali and charge ordering, as well as slab gliding that leads to new stacking and structures.[2,11,25,49,50] The electrochemical curves corresponding to the cells used for the preparation of the *ex situ* samples show these specific features, demonstrating high reproducibility (Fig. S1†).

The XRD patterns of pristine and electrochemically deintercalated LNO electrodes are presented in Fig. 2b. Rietveld refinements, performed to describe the changes in the layered structure of LNO upon Li$^+$ extraction, confirm the reliability of the materials based on reported results (see the appendix for more details on the refinements, Tables S1.0–S1.5†). The refinement of the pattern of pristine LNO, sample X0, resulted in a slightly non-stoichiometric composition of $Li_{0.97}Ni_{1.03}O_2$ with 0.03 Ni^{2+} in the Li site, balanced by the presence of 0.03 Ni^{2+} in the Ni sites and 0.97 Ni^{3+} ($z = 0.033(2)$ in $Li_{1-z}Ni_{1+z}O_2$, Table S1.0†). Upon Li$^+$ deintercalation, significant changes in the XRD patterns occurred, including the emergence of a biphasic state with a new monoclinic phase (M), confirmed by the splitting of 101 and 104 reflections as shown in Fig. 2b. Further delithiation resulted in the expected phase transition back to a hexagonal phase (H), aligning with previously reported work especially at highly delithiated states.[6,13,25,50,51] The evolution of phases and their corresponding contributions are summarized in Fig. S2.†

Structurally, Li$^+$ deintercalation leads to the expected trends in cell parameters and cell volume. A contraction in the *a/b* cell parameters reflects the oxidation of nickel transition metal
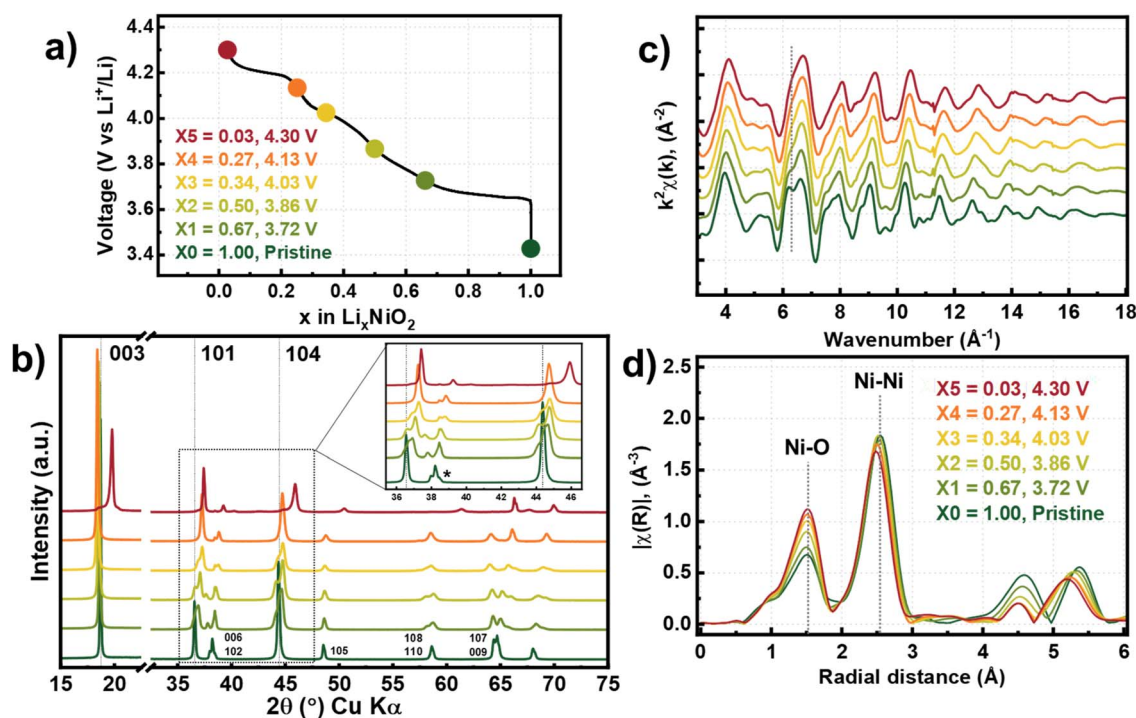

Fig. 2 (a) The first electrochemical charge curve obtained for the LNO electrode material *vs.* Li metal; the different compositions studied in the following are highlighted and obtained at different cut-off voltages and (b) the evolution in the XRD patterns between the pristine LNO material and the electrochemically deintercalated electrodes, with the inset highlighting the splitting of the 101 and 104 reflections. An asterisk is added in the inset which corresponds to the Al 111 reflection at about 38.5°; (c) the k^2-weighted EXAFS oscillations extracted at the Ni K-edge and (d) the magnitude of the Fourier transform (FT) of the EXAFS oscillations (uncorrected with the phase shift).
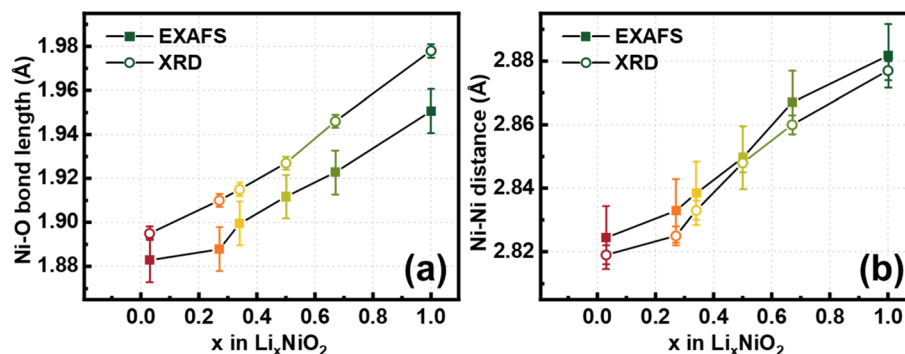
Fig. 3 (a) The Ni–O and (b) Ni–Ni atomic distances determined from EXAFS and XRD analyses.

ions, inducing shortened Ni–O and Ni–Ni atomic distances (Table S2†), consistent with the increasing covalency of the Ni–O framework. Meanwhile, up to the extraction of about 0.65 Li$^+$ ions, an expansion in the c parameter is observed despite the decreasing thickness of the NiO$_2$ slabs. This effect reflects the increased repulsive forces between oxygen layers across the interslab space as the deintercalated Li$^+$ ions no longer play their stabilization and screening role. This expansion is then followed by a decrease due to a change in the slabs stacking promoted by the covalency of the Ni–O network, as previously reported.[11,25,50]

The Rietveld refinements provide an average description of the Ni environment based on the long-range structure, as summarized in Table S2.† In this regard, it should be noted that the crystal symmetry, whether monoclinic or hexagonal, impacts the description of the local Ni structure and in particular the average Ni–O bond length. For samples containing two crystallographic phases, their weight fractions were used to calculate the average Ni–O and Ni–Ni distances. These values can be compared with those obtained from the analysis of the EXAFS spectra. This enables a more precise evaluation of the long-range and of the local environments of Ni, particularly in cases where local distortions might exist.

The k^2-weighted EXAFS oscillations show a steady evolution of the local structure as delithiation progresses (Fig. 2c), especially at low wavenumbers between 5 and 10 Å^{-1}. These changes are reflected in the Fourier transform of the EXAFS oscillations, representing the partial local structural distribution around the absorber Ni site, where two main peaks are identified, corresponding to the Ni–O and Ni–Ni atomic distances (Fig. 2d). Moreover, the high k-value used to extract the EXAFS oscillations would result in a better resolution in the R space ($\Delta R = \pi/2 \times k_{max} = 0.09$ Å), thus enabling a more accurate description of the local structure of the Li$_x$NiO$_2$ compounds. A progressive increase in the intensity of the Ni–O peak and a slight shift to lower radial distances, accompanied by reduced Ni–Ni peak intensity, are observed. Following the phase transformations (H1 → M → H2 → H3) obtained from XRD analysis, EXAFS fitting models using 6 equivalent Ni–O distances for H phase-dominated samples and [4 + 2] Ni–O distances for M phase-dominated samples for the Ni–O bonds and six equivalent Ni–Ni atomic distances lead to reasonable fits for all samples (Fig.

S3†). This simple model should be sufficient to account for possible general structural distortions occurring in the material.[15,16,19] Concerning the pristine LiNiO$_2$ material, the distortion in the NiO$_6$ octahedra is expected for Ni^{3+}, leading to changes in the electronic configuration due to JT distortion. Similarly, a degree of BD states due to the mixed valence between Ni^{2+} and Ni^{3+} may also occur in the pristine material. Moreover, a possible local distortion around Ni ([4 + 2] Ni–O distances) was therefore also considered in the H-type structure, but its occurrence could not be clearly assessed, in line with the results of a recent XAS study.[26] It is important to note that this model also yielded an acceptable fit. More importantly, using the models [6, Ni–O for H phase] and [4 + 2, Ni–O for M phase] resulted in Ni–O bond distances which align well with the sum of the ionic radii ($r_{Ni^{3+}} = 0.56$ Å, $r_{Ni^{4+}} = 0.48$ Å, and $r_{O^{2-}} = 1.40$ Å), especially for the pristine (∼1.96 Å) and highly delithiated samples (∼1.88 Å), supporting the general trend observed by both XRD and EXAFS (Fig. 3).[13] A summary of the EXAFS results is shown in Table S3.†

3.2 The charge compensation mechanism in LiNiO$_2$ and effect of covalency

The evolution of the bulk oxidation state of Ni was followed by analyzing the *ex situ* Ni K-edge XANES spectra of the pristine and cycled LNO samples (Fig. 4a). A gradual continuous shift of the main peak and a rising edge position towards higher energy (from 8347.5 eV to about 8348.2 eV at $J = 0.8$, where J is the normalized intensity at the edge jump) are observed along the series. However, at cut-off voltages of 4.03 and 4.13 V (samples X3/X4), a break in the trend is observed (Fig. 4b). Moreover, at the highest cut-off voltage of 4.30 V (sample X5), a different slope of the rising edge is observed (Fig. 4c). These observations suggest that the shift of the rising edge position cannot be used to directly assess the Ni electronic state, proving a more complex relationship between the rising edge position and the Ni oxidation state. Indeed, it is important to recall that the XANES features do not solely reflect the density of unoccupied states above the Fermi level, but they also depend on the local orbital rearrangement.[52]

Meanwhile, the pre-edge intensity slightly increases and shifts to higher energy upon Li$^+$ ion extraction (Fig. 4d). An increasing pre-edge intensity is expected due to the removal of
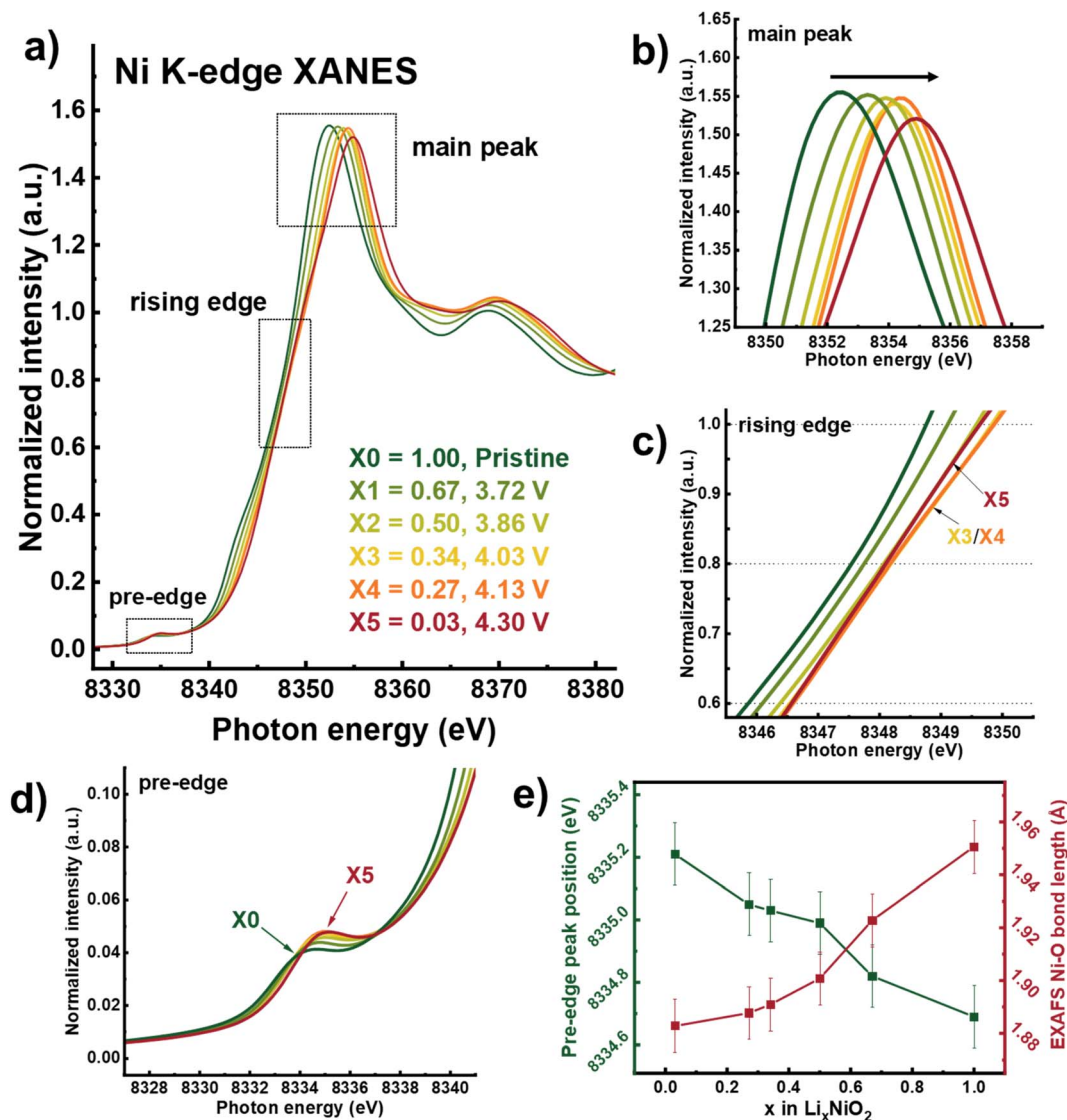
Fig. 4 (a) Ni K-edge XANES spectra of the pristine and the electrochemically deintercalated LNO electrodes, highlighting the evolution of (b) the main peak, (c) the edge position, and (d) the pre-edge region; (e) the correlation between the Ni–O average bond distances from EXAFS and the pre-edge peak position.

electrons from nickel 3d orbitals. In addition, the increased hybridization may be directly correlated with the increasing covalent framework consequent to the shortening of the Ni–O bond distances, resulting in a mild overlap between orbitals especially when local distortions are expected (e.g., for the M phase more than for the H phase). Subsequently, the observed pre-edge features support the increase in the Ni oxidation state because of these local structural and electronic changes. A strong correlation is evident in Fig. 4e between the pre-edge peak position and the Ni–O bond distances from EXAFS analysis as a function of the expected Li^+ ion composition.[6,25,50,53] It is also important to note that the evolution of the pre-edge signals shows no indication of a possible tetrahedral coordination of Ni in the Li layer, as previously reported.[54]

While the Ni K-edge XANES energy position in the series of samples obtained upon Li^+ ion deintercalation generally evolves

continuously with the expected oxidation of Ni, a more complex evolution is observed depending on the feature being examined, which may be likely connected to the increased covalency of Ni–O bonds. Thus, the rising edge position alone may not be sufficient to accurately determine the oxidation state of Ni, as it can be influenced by the nature of the Ni–O bonds.[23] To address this, Ni CtC and VtC Kβ XES was used as a complementary technique (Fig. 5a). In fact, the Ni CtC Kβ XES line (8225–8300 eV) results from the specific electronic relaxation process corresponding to $3p \rightarrow 1s$ transition filling the Ni core-hole. The main emission line, corresponding to the CtC $K\beta_{1,3}$ region, is highly sensitive to the electronic environment, particularly the valence electrons, due to the strong 3p–3d exchange interaction, and is expected to provide insights into the electrons from the occupied states. It is apparent that a significant shift towards higher energies is observed on going from divalent NiO
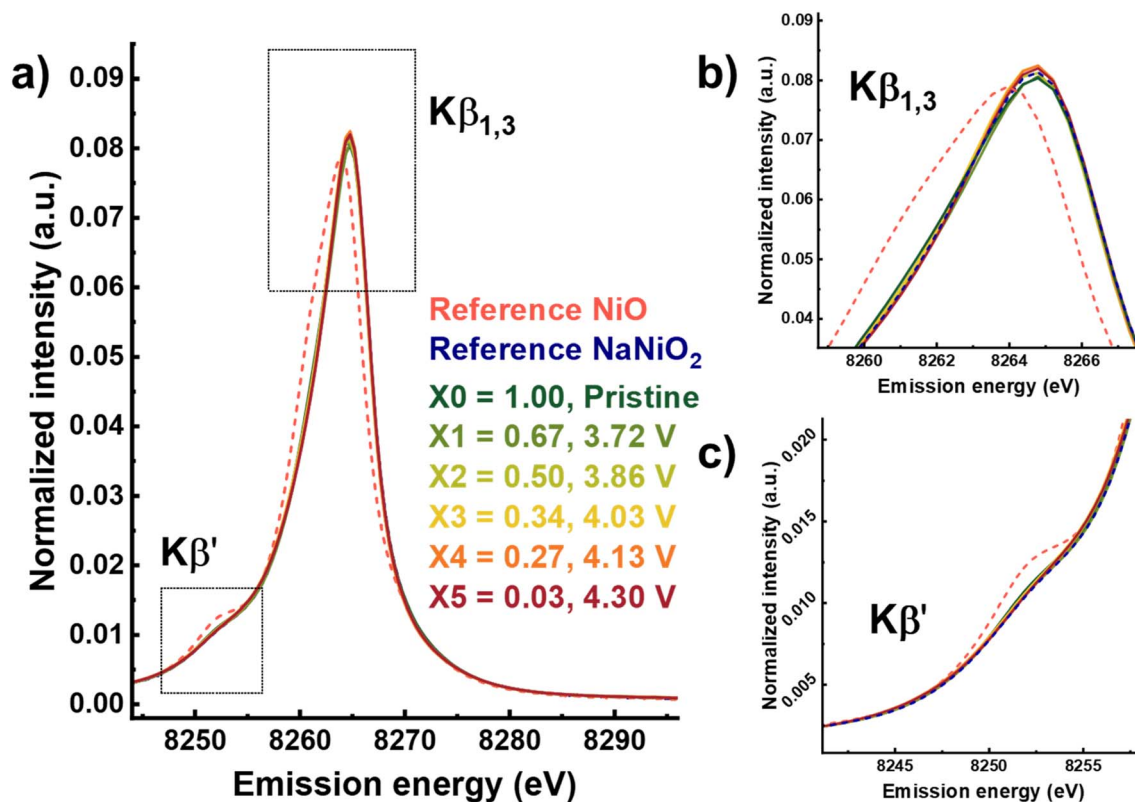
Fig. 5 (a) Ni Kβ X-ray emission lines of the pristine and electrochemically delithiated LNO positive electrodes, highlighting (b) the CtC $K\beta_{1,3}$ region and (c) the CtC $K\beta'$ region. Reference materials, NiO (Ni^{2+}: d^8) and $NaNiO_2$ (Ni^{3+}: d^7), are included for better comparison.

($\sim$8264.3 eV) to trivalent $LiNiO_2$ ($\sim$8264.9 eV) and $NaNiO_2$ ($\sim$8264.8 eV), despite a shift towards lower emission energies being expected as the oxidation state increases as similarly observed for several transition metals (Ti, V, Cr, Mn, Fe, and Co).[55,56] Limited reports have been published in the case of Ni and such trends are still under investigation. Moreover, no clear shift can be detected for the delithiated materials (Fig. 5b). Additionally, it should be noted that the CtC $K\beta'$ region is also of interest because it reflects the overall spin state.[57] In an ionic description of the Ni electronic and spin state for the Li_xNiO_2 compounds, the overall spin state should change from $S = 1/2$ (Ni^{3+}: d^7) to $S = 0$ (Ni^{4+}: d^6), resulting in a decrease in the d-count which corresponds to the decrease in the net spin state.[42] However, no visible alteration is observed suggesting that there is no change in the local magnetic moment across the materials relative to that of a high spin NiO with $S = 1$ (Ni^{2+}: d^8) (Fig. 5c).

Quantitatively, the integrated absolute difference (IAD) within a range of energy can be of help for such evaluation, as reported in previous studies.[42,58,59] The IAD provides insights into the local magnetic moment deriving from the electronic environment and is independent of structural effects in the material.[42] As the IAD values can directly be correlated with the unpaired electrons in the filled 3d states they should also be sensitive to the overall oxidation state of Ni.[42] Therefore, the IAD values over a range covering the Ni CtC Kβ emission lines were calculated with the reference NiO material set as the reference

(IAD = 0). For simplicity, the formal oxidation states of pristine and electrochemically delithiated LNO samples, which were mainly based on ionic charge balance given that a certain amount of Li^+ ions was extracted, are correlated with the calculated IAD as seen in Fig. 6. Note that the formal oxidation state is not an appropriate descriptor of the electronic configuration in a covalent system, as it is defined in a pure ionic picture. Interestingly, the calculated IAD values are very similar
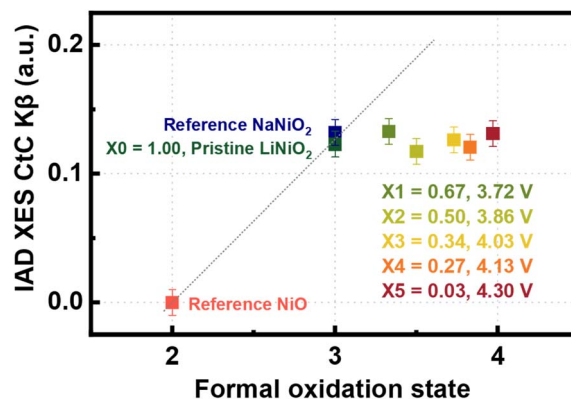

Fig. 6 The result of the IAD analysis over the energy range 8200–8300 eV with the reference NiO set as IAD = 0. A line connecting the reference NiO and $NaNiO_2$ is presented as a guide for the expected slope in the increase of the formal oxidation state.

for all the Li_xNiO_2 samples (0.11 to 0.13 $\pm$ 0.01) which suggests that the overall electronic environment in LNO does not have a significant change despite the removal of Li^+ ions, confirming the covalent nature of the Ni–O bonds.[58] This means that strong metal–ligand covalency delocalizes the 3d electrons, reducing the effective exchange interactions, resulting in unchanged IAD values. Furthermore, covalency redistributes electron density but does not alter the total number of unpaired electrons if the spin state is preserved.

On the other hand, the Ni VtC $K\beta$ XES (8300–8350 eV) (Fig. S4a†) is highly sensitive to the chemical properties of the ligands coordinated to the absorber atom.[41] This emission line displays high correlation and agreement with the local bond distances obtained from EXAFS analysis (Fig. S4b†).[48,56,60,61] As Li^+ ions are extracted from the bulk LNO, a subtle but significant shift in the main peak at ~8327 eV towards higher energy is observed. The shortest Ni–O bond distance obtained from XRD analysis of ~1.8876(3) Å and from EXAFS fitting of ~1.88(1) Å corresponds to the higher emission energy (Tables S2 and S3†). The main peak of the Ni $K\beta_{2,5}$ emission line is directly correlated with the average Ni–O bond distances from XRD and EXAFS refinements, proving that the VtC XES can also be used to assess the structural evolution of positive electrode materials.[48]

Generally, the determination of the oxidation state by probing the unoccupied electronic states through Ni K-edge XANES spectra suggests an increase in the Ni oxidation state, at least up to 4.03 V. Furthermore, the analysis of the occupied electronic states from Ni CtC $K\beta$ XES spectra by the IAD method indicates that the number of unpaired electrons may not actually be decreasing in the series of samples. This suggests the presence of a strong covalent interaction within the NiO_6 framework throughout the delithiation process. Therefore, despite having a clear decrease in bond distances between the Ni and O atoms (Tables S2 and S3†), combined results from XANES and XES suggest a strong charge transfer process between the Ni 3d and O 2p states, affecting the overall electronic environment and the charge compensation process upon Li^+ ion extraction.[21]

The question now centers on understanding the relationship between Ni and O in LNO, considering both their oxidation states as Li^+ ions are extracted. In this line, it is essential to extract direct information on the Ni 3d–O 2p electronic interaction. For this purpose, Ni $L_{2,3}$-edges XRS and the O K-edge XRS spectra were collected on the same series of electrochemically delithiated LNO electrodes (Fig. 7a and b).

The oxidation state of Ni can be assessed by looking into the Ni $L_{2,3}$-edges XRS, corresponding to the dipole electronic transition from the occupied Ni 2p to the unoccupied Ni 3d states. Overall characteristic features including a double peak at lower energies, at ~853.7 eV (peak A) and at ~855.4 eV (peak B), and another feature at higher energies at ~872.5 eV (peak C) are consistent with Ni $L_{2,3}$-edges spectra obtained from soft-XAS in previous studies.[27,28] Specifically, the former is assigned to the Ni L_3-edge (peaks A and B: $2p_{3/2} \rightarrow 3d$), while the latter is for the L_2-edge (peak C: $2p_{1/2} \rightarrow 3d$). Generally, a bimodal splitting feature of about 2 eV can only be observed at the L_3-edge and only as
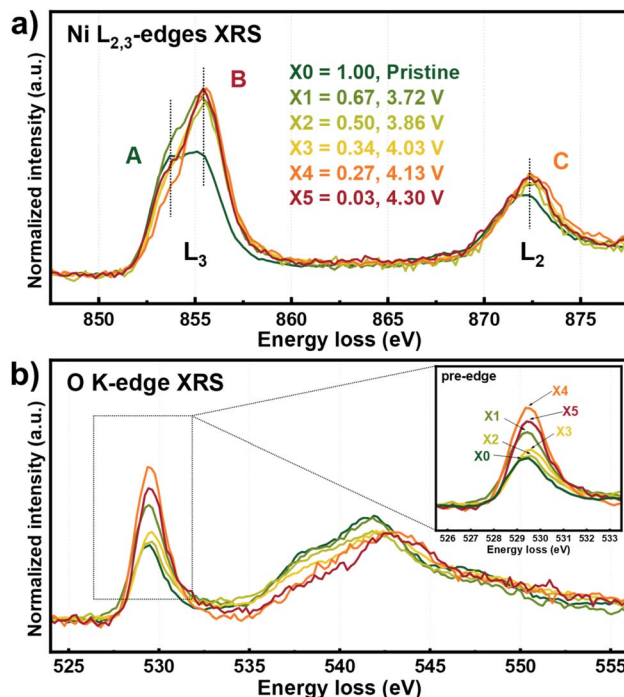

Fig. 7 (a) Ni $L_{2,3}$-edges and (b) O K-edge XRS spectra of the pristine and electrochemically delithiated LNO positive electrodes.

a slightly broad feature at the L_2-edge, especially for X0. Moreover, it should be noted that differences in the probing depth entail distinct features as soft-XAS is typically limited to 100 nm (using fluorescence yield detection), whereas XRS enables probing depths up to 10 μm, thus probing the bulk of the material.[62] Upon delithiation, peak B gradually increases in intensity, with diminishing features at peak A, although this trend is not linearly dependent on the amount of deintercalated Li^+ ions. Thus, it can be inferred that peak B becomes more intense for more oxidized samples. This sharp main feature at an energy equivalent to ~855.4 eV is typically assigned to highly oxidized Ni (formal oxidation state +4), commonly seen in $KNi^{IV}IO_6$.[63,64] Previous reports on the Ni $L_{2,3}$-edges for LNO materials confirm the same.[26,27] Intriguingly, a broader shoulder at peak A is observed from sample X5, while a less pronounced feature is observed in sample X4, despite both having intense features at peak B, which could signify partial reduction of Ni. Overall, it is compelling that the general observation of the changes in the Ni $L_{2,3}$-edges XRS would require further quantitative analysis and the possibility for theoretical studies to further elucidate the dynamic changes in the electronic environment. Nevertheless, the results obtained in probing the Ni electronic environment from the Ni K-edge XAS, Ni CtC $K\beta$ XES, and Ni $L_{2,3}$-edge XRS confirm the complex interplay between Ni–O bonds.

The O K-edge XRS spectra exhibit two distinct regions: the pre-edge, with the most intense feature at around ~529.5 eV and a broader feature 5–10 eV above the pre-edge, corresponding to the oxygen p-character hybridized with the 4s and 4p orbitals of Ni (Fig. 7b).[65,66] The pre-edge reveals changes in the electronic environment of oxygen due to strong hybridization

between the Ni 3d and O 2p orbitals. Our results reveal clear changes in the pre-edge feature upon delithiation, as seen in the increased intensity in comparison to that of the pristine material (inset of Fig. 7b), and show more resolved features in contrast to the previously reported O K-edge soft-XAS results showing only relatively small changes in intensity.[27] In relation to the pre-edge intensity, a recent O K-edge XRS study, supported by *ab initio* calculations, reported that reproducing the intense pre-edge feature requires increased overlap between the O 2p and Ni 3d orbitals, implying higher Ni–O bond covalency.[26] The increased hybridization is clearly observed across the series, enabling electron transfer from the O 2p ligands to the Ni 3d orbitals, leaving ligand holes for lattice oxygen activation.[21,67–69] This is further supported by the charge redistribution between oxygen and nickel atoms at high voltage in the highly delithiated state, suggesting the participation of oxygen holes in the charge compensation mechanism.[26] Similar strong charge transfer effects within the hybridized Co 3d and O 2p orbitals of the Co–O bonds in $LiCoO_2$ positive electrodes, especially at high states of charge, were recently reported by Asakura and co-workers wherein a partially reduced Co environment was observed as a consequence of the presence of ligand holes in the oxygen orbitals.[70] This is in line with the possibly covalent CoO_2 network resulting in a negative charge transfer from O 2p to Co 3d orbitals, which plays an important role in the charge compensation mechanism.

Furthermore, the integrated oxygen XRS pre-edge area increases during Li^+ ion deintercalation, followed by a decrease, and then a subsequent increase (Fig. 8). Notably, samples X2 and X3, both purely monoclinic with a distortion of the

triangular oxygen lattice compared to the hexagonal phases, as well as X5, characterized by a different oxygen stacking (O1-type in H3 *versus* O3-type in H1/H2/M),[25] show a decrease in pre-edge intensity. This implies that, as phase transitions occur upon delithiation, the overall crystallographic structure may also impact, on average, the Ni–O bond covalency. Otherwise, this decrease in covalency may also be related to the local Li vacancy ordering affecting the Ni–O covalency in the local structure.[12,25] A systematic and detailed theoretical study is needed to further elucidate such a decrease in covalency in the monoclinic phase, to determine whether it is related to the long-range structure or local geometric environment, or to both effects.

These findings provide original insights into the possible relationships among structural phase transitions, electronic properties, covalency and Ni–O bond distances, shedding new light on the role of nickel and oxygen in the charge compensation process. The results suggest that changes in covalency may occur independently of the Ni–O bond distances and could mainly rely on the electronic structure of LNO. Furthermore, an induced negative charge transfer to the Ni 3d environment from the O 2p states is confirmed, producing ligand holes in the oxygen orbitals.[21,23,31,71]

Based on the presence of such ligand holes in $LiNiO_2$, its initial electronic configuration could be better described by $3d^{7+n} L^n$ (L indicates one hole in the ligand site) states instead of the conventional low spin $3d^7$ ones, implying the dynamic interplay between Ni and O, which influences the overall electronic environment.[23] Furthermore, as more Li^+ ions are deintercalated, the 3d orbital of Ni lowers in energy, resulting in an increased overlap with the 2p orbital of the oxide ion, further stabilizing the $3d^{6+n} L^n$ (where $0 > n > 2$) configuration and resulting in the formation of ligand holes.[21,23,26,70,72] Covalency is expected to increase with greater overlap between the 2p and 3d orbitals, which is typically associated with shorter metal-oxide bond lengths. This work, however, reveals a more complex interplay, showing that covalency is also influenced by the evolution of the average long-range structure.

4 Conclusion

A comprehensive correlative analysis of the long-range and local structure of pristine and electrochemically delithiated LNO positive electrodes was carried out through *ex situ* XRD and EXAFS studies. Additional insights into the bulk electronic structure of LNO at different states of charge are obtained using complementary hard X-ray spectroscopic techniques. Moreover, the proposed experimental workflow relying on the use of the same samples and varying conditions of spectral collection, excluding beam-induced damage, not only eliminates potential discrepancies in the uniformity of the materials used but also demonstrates the reliability and reproducibility of the results.

Specifically, Ni K-edge XAS allows following the evolution of the electronic environment of Ni, aligning with structural changes observed in the EXAFS analysis and consistent with XRD refinements. This highlights how the local coordination of Ni within the NiO_2 slabs evolves during delithiation. Moreover, the findings from the Ni CtC Kβ XES through IAD analysis suggest
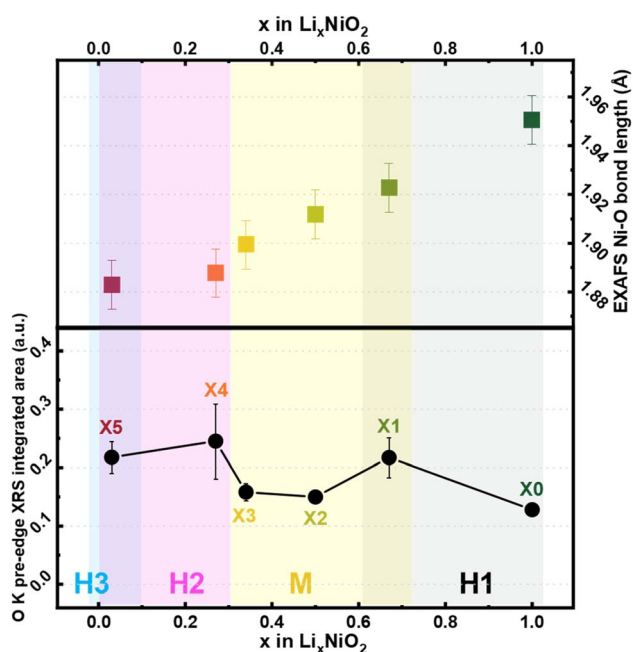

Fig. 8 The correlation between (top) the local Ni–O bond distances from EXAFS analysis and (bottom) the integrated area of the pre-edge of the O K-edge XRS spectra. Highlighted areas correspond to the global crystal phases indicated by H1, M, H2, and H3.

that a strong influence on the covalency in the Ni–O bonds may exist across samples. In addition, Ni $L_{2,3}$-edges XRS further clarifies the role of Ni in the charge compensation mechanism. The strong involvement of oxygen in the charge compensation process during the delithiation is also confirmed by O K-edge XRS. The combination of these techniques allows probing the covalent nature of the Ni–O bonds, which induces a stronger reductive effect, especially at high potential. In particular, the covalent nature of the Ni–O bonds, in pristine as well as in delithiated LNO, appears very complex, being influenced not only by the local Ni–O environment but also by the long-range structure. The latter involves differences in oxygen packing, NiO_2 slab interlayer interaction and Li/vacancy ordering, but also possible distortions of the oxygen triangular lattice.

These findings imply that understanding the interplay between the local and the long-range structural changes is crucial for unraveling the charge compensation mechanisms in LNO. Theoretical studies, particularly focused on the relationship between the short- and the long-range structural ordering, are therefore necessary to fully describe and correlate the structural and electronic environment in a similar class of materials. These studies would extend our understanding of the interaction between covalency and structural phase transitions during the delithiation process, offering valuable insights into Ni-rich positive electrode materials. This improved understanding is mandatory to shed light on their contribution to the development of more efficient and stable electrode materials.

Data availability

We certify that the data corresponding to the results reported in our paper "Insights into the role of the covalent Ni–O bonds in $LiNiO_2$ positive electrodes: a correlative hard X-ray spectroscopy study" by Togonon *et al.* will be available when asked, including those mentioned in the manuscript and also in the ESI.†

Author contributions

Conflicts of interest

There are no conflicts to declare.

Acknowledgements

References

1 N. Nitta, F. Wu, J. T. Lee and G. Yushin, Li-ion battery materials: Present and future, *Mater. Today*, 2015, **18**, 252–264, DOI: **10.1016/j.mattod.2014.10.040**.

2 H. Li, N. Zhang, J. Li and J. R. Dahn, Updating the Structure and Electrochemistry of Li x NiO 2 for $0 \leq x \leq 1$, *J. Electrochem. Soc.*, 2018, **165**, A2985–A2993, DOI: **10.1149/2.0381813jes**.

3 C. Xu, K. Märker, J. Lee, A. Mahadevogowda, P. J. Reeves, S. J. Day, M. F. Groh, S. P. Emge, C. Ducati, B. Layla Mehdi, C. C. Tang and C. P. Grey, Bulk fatigue induced by surface reconstruction in layered Ni-rich cathodes for Li-ion batteries, *Nat. Mater.*, 2021, **20**, 84–92, DOI: **10.1038/s41563-020-0767-8**.

4 K. McColl, R. A. House, G. J. Rees, A. G. Squires, S. W. Coles, P. G. Bruce, B. J. Morgan and M. S. Islam, Transition metal migration and O2 formation underpin voltage hysteresis in oxygen-redox disordered rocksalt cathodes, *Nat. Commun.*, 2022, **13**, 5275, DOI: **10.1038/s41467-022-32983-w**.

5 H. H. Ryu, H. H. Sun, S. T. Myung, C. S. Yoon and Y. K. Sun, Reducing cobalt from lithium-ion batteries for the electric vehicle era, *Energy Environ. Sci.*, 2021, **14**, 844–852, DOI: **10.1039/d0ee03581e**.

6 M. Bianchini, M. Roca-Ayats, P. Hartmann, T. Brezesinski and J. Janek, There and Back Again—The Journey of LiNiO2 as a Cathode Active Material, *Angew. Chem., Int. Ed.*, 2019, **58**, 10434–10458, DOI: **10.1002/anie.201812472**.

7 L. de Biasi, A. Schiele, M. Roca-Ayats, G. Garcia, T. Brezesinski, P. Hartmann and J. Janek, Phase Transformation Behavior and Stability of LiNiO2 Cathode Material for Li-Ion Batteries Obtained from In Situ Gas Analysis and Operando X-Ray Diffraction, *ChemSusChem*, 2019, **12**, 2240–2250, DOI: **10.1002/cssc.201900032**.

8 A. O. Kondrakov, H. Geßwein, K. Galdina, L. De Biasi, V. Meded, E. O. Filatova, G. Schumacher, W. Wenzel, P. Hartmann, T. Brezesinski and J. Janek, Charge-transfer-induced lattice collapse in Ni-rich NCM cathode materials

during delithiation, *J. Phys. Chem. C*, 2017, **121**, 24381–24388, DOI: **10.1021/acs.jpcc.7b06598**.

9 E. Bautista Quisbert, F. Fauth, A. M. Abakumov, M. Blangero, M. Guignard and C. Delmas, Understanding the High Voltage Behavior of LiNiO2 Through the Electrochemical Properties of the Surface Layer, *Small*, 2023, **19**(30), 2300616, DOI: **10.1002/smll.202300616**.

10 C. Delmas, J. P. Peres, A. Rougier, A. Demourgues, F. Weill, A. V. Chadwick, M. Broussely, F. Perton, P. Biensan and P. Willmann, On the behavior of the LixNiO2 system: An electrochemical and structural overview, *J. Power Sources*, 1997, **68**, 120–125, DOI: **10.1016/S0378-7753(97)02664-5**.

11 A. Rougier, P. Gravereau and C. Delmas, Optimization of the Composition of the Li1 − z Ni1 + z O 2 Electrode Materials: Structural, Magnetic, and Electrochemical Studies, *J. Electrochem. Soc.*, 1996, **143**, 1168–1175, DOI: **10.1149/1.1836614**.

12 J. P. Peres, A. Demourgues and C. Delmas, Structural investigations on Li0.65−Ni1+O2 cathode material: XRD and EXAFS studies, *Solid State Ionics*, 1998, **111**, 135–144, DOI: **10.1016/S0167-2738(98)00122-2**.

13 A. N. Mansour, X. Q. Yang, X. Sun, J. McBreen, L. Croguennec and C. Delmas, In Situ X-Ray Absorption Spectroscopy Study of Li[sub (1−z)]Ni[sub (1+z)]O[sub 2] (z ≤ 0.02) Cathode Material, *J. Electrochem. Soc.*, 2000, **147**, 2104, DOI: **10.1149/1.1393492**.

14 C. Delmas, M. Ménétrier, L. Croguennec, I. Saadoune, A. Rougier, C. Pouillerie, G. Prado, M. Grüne and L. Fournes, An overview of the Li(Ni,M)O2 systems: Syntheses, structures and properties, *Electrochim. Acta*, 1999, **45**, 243–253, DOI: **10.1016/S0013-4686(99)00208-X**.

15 H. Chen, C. L. Freeman and J. H. Harding, Charge disproportionation and Jahn-Teller distortion in LiNiO2 and NaNiO2: A density functional theory study, *Phys. Rev. B:Condens. Matter Mater. Phys.*, 2011, **84**, 1–7, DOI: **10.1103/PhysRevB.84.085108**.

16 K. Foyevtsova, I. Elfimov, J. Rottler and G. A. Sawatzky, LiNiO2 as a high-entropy charge- and bond-disproportionated glass, *Phys. Rev. B*, 2019, **100**, 1–7, DOI: **10.1103/PhysRevB.100.165104**.

17 S. Sicolo, M. Mock, M. Bianchini and K. Albe, And Yet It Moves: LiNiO2, a Dynamic Jahn-Teller System, *Chem. Mater.*, 2020, **32**, 10096–10103, DOI: **10.1021/acs.chemmater.0c03442**.

18 J. H. Chung, T. Proffen, S. Shamoto, A. M. Ghorayeb, L. Croguennec, W. Tian, B. C. Sales, R. Jin, D. Mandrus and T. Egami, Local structure of LiNiO 2 studied by neutron diffraction, *Phys. Rev. B:Condens. Matter Mater. Phys.*, 2005, **71**, 8–11, DOI: **10.1103/PhysRevB.71.064410**.

19 A. Rougier, C. Delmas and A. V. Chadwick, Non-cooperative Jahn-Teller effect in LiNiO2: An EXAFS study, *Solid State Commun.*, 1995, **94**, 123–127, DOI: **10.1016/0038-1098(95)00020-8**.

20 N. Li, S. Sallis, J. K. Papp, J. Wei, B. D. McCloskey, W. Yang and W. Tong, Unraveling the Cationic and Anionic Redox Reactions in a Conventional Layered Oxide Cathode, *ACS Energy Lett.*, 2019, **4**, 2836–2842, DOI: **10.1021/acsenergylett.9b02147**.

21 H. Huang, Y. C. Chang, Y. C. Huang, L. Li, A. C. Komarek, L. H. Tjeng, Y. Orikasa, C. W. Pao, T. S. Chan, J. M. Chen, S. C. Haw, J. Zhou, Y. Wang, H. J. Lin, C. Te Chen, C. L. Dong, C. Y. Kuo, J. Q. Wang, Z. Hu and L. Zhang, Unusual double ligand holes as catalytic active sites in LiNiO2, *Nat. Commun.*, 2023, **14**, 1–14, DOI: **10.1038/s41467-023-37775-4**.

22 D. M. Korotin, D. Novoselov and V. I. Anisimov, Paraorbital ground state of the trivalent Ni ion in LiNiO2 from DFT+DMFT calculations, *Phys. Rev. B*, 2019, **99**, 1–6, DOI: **10.1103/PhysRevB.99.045106**.

23 A. R. Genreith-Schriever, H. Banerjee, A. S. Menon, E. N. Bassey, L. F. J. Piper, C. P. Grey and A. J. Morris, Oxygen hole formation controls stability in LiNiO2 cathodes, *Joule*, 2023, **7**, 1623–1640, DOI: **10.1016/j.joule.2023.06.017**.

24 R. A. House, G. J. Rees, M. A. Pérez-Osorio, J. J. Marie, E. Boivin, A. W. Robertson, A. Nag, M. Garcia-Fernandez, K. J. Zhou and P. G. Bruce, First-cycle voltage hysteresis in Li-rich 3d cathodes associated with molecular O2 trapped in the bulk, *Nat. Energy*, 2020, **5**, 777–785, DOI: **10.1038/s41560-020-00697-2**.

25 L. Croguennec, C. Pouillerie, A. N. Mansour and C. Delmas, Structural characterisation of the highly deintercalated LixNi1.02O2 phases (with x≤0.30), *J. Mater. Chem.*, 2001, **11**, 131–141, DOI: **10.1039/b003377o**.

26 Q. Jacquet, N. Mozzhukhina, P. N. O. Gillespie, G. Wittmann, L. P. Ramirez, F. G. Capone, J. P. Rueff, S. Belin, R. Dedryvère, L. Stievano, A. Matic, E. Suard, N. B. Brookes, A. Longo, D. Prezzi, S. Lyonnard and A. Iadecola, A Fundamental Correlative Spectroscopic Study on Li1-xNiO2 and NaNiO2, *Adv. Energy Mater.*, 2024, 2401413, DOI: **10.1002/aenm.202401413**.

27 W. S. Yoon, K. Y. Chung, J. McBreen, D. A. Fischer and X. Q. Yang, Changes in electronic structure of the electrochemically Li-ion deintercalated LiNiO2 system investigated by soft X-ray absorption spectroscopy, *J. Power Sources*, 2006, **163**, 234–237, DOI: **10.1016/j.jpowsour.2006.02.013**.

28 W. S. Yoon, M. Balasubramanian, K. Y. Chung, X. Q. Yang, J. McBreen, C. P. Grey and D. A. Fischer, Investigation of the charge compensation mechanism on the electrochemically Li-ion deintercalated Li1-xCo1/3Ni1/3Mn1/3O2 electrode system by combination of soft and hard X-ray absorption spectroscopy, *J. Am. Chem. Soc.*, 2005, **127**, 17479–17487, DOI: **10.1021/ja0530568**.

29 Y. Koyama, T. Mizoguchi, H. Ikeno and I. Tanaka, Electronic structure of lithium nickel oxides by electron energy loss spectroscopy, *J. Phys. Chem. B*, 2005, **109**, 10749–10755, DOI: **10.1021/jp050486b**.

30 H. Ikeno, I. Tanaka, Y. Koyama, T. Mizoguchi and K. Ogasawara, First-principles multielectron calculations of Ni L2,3 NEXAFS and ELNES for LiNi O2 and related compounds, *Phys. Rev. B:Condens. Matter Mater. Phys.*, 2005, **72**, 1–8, DOI: **10.1103/PhysRevB.72.075123**.

31 R. Fantin, T. Jousseaume, R. Ramos, G. Lefevre, A. Van Roekeghem, J. P. Rueff and A. Benayad, Depth-Resolving the Charge Compensation Mechanism from LiNiO2 to NiO2, *ACS Energy Lett.*, 2024, **9**, 1507–1515, DOI: **10.1021/acsenergylett.4c00360**.

32 A. S. Menon, B. J. Johnston, S. G. Booth, L. Zhang, K. Kress, B. E. Murdock, G. Paez Fajardo, N. N. Anthonisamy, N. Tapia-Ruiz, S. Agrestini, M. Garcia-Fernandez, K. Zhou, P. K. Thakur, T. L. Lee, A. J. Nedoma, S. A. Cussen and L. F. J. Piper, Oxygen-Redox Activity in Non-Lithium-Excess Tungsten-Doped Li Ni O 2 Cathode, *PRX Energy*, 2023, **2**(1), 013005, DOI: **10.1103/prxenergy.2.013005.**

33 X. Gao, B. Li, K. Kummer, A. Geondzhian, D. A. Aksyonov, R. Dedryvère, D. Foix, G. Rousse, M. Ben Yahia, M. Doublet, A. M. Abakumov and J. Tarascon, Clarifying the origin of molecular O2 in cathode oxides, *Nat. Mater.*, 2025, **24**(5), 743–752, DOI: **10.1038/s41563-025-02144-7**.

34 C. J. Sahle, A. Mirone, J. Niskanen, J. Inkinen, M. Krisch and S. Huotari, Planning, performing and analyzing X-ray Raman scattering experiments, *J. Synchrotron Radiat.*, 2015, **22**, 400–409, DOI: **10.1107/S1600577514027581**.

35 R. Georgiou, C. J. Sahle, D. Sokaras, S. Bernard, U. Bergmann, J. P. Rueff and L. Bertrand, X-ray Raman Scattering: A Hard X-ray Probe of Complex Organic Systems, *Chem. Rev.*, 2022, **122**, 12977–13005, DOI: **10.1021/acs.chemrev.1c00953**.

36 K. Tohji and Y. Udagawa, X-ray Raman scattering as a substitute for soft-x-ray extended x-ray-absorption fine structure, *Phys. Rev. B:Condens. Matter Mater. Phys.*, 1989, **39**, 7590–7594, DOI: **10.1103/PhysRevB.39.7590**.

37 D. Sokaras, D. Nordlund, T. C. Weng, R. A. Mori, P. Velikov, D. Wenger, A. Garachtchenko, M. George, V. Borzenets, B. Johnson, Q. Qian, T. Rabedeau and U. Bergmann, A high resolution and large solid angle x-ray Raman spectroscopy end-station at the Stanford Synchrotron Radiation Lightsource, *Rev. Sci. Instrum.*, 2012, **83**, 043112, DOI: **10.1063/1.4704458**.

38 A. P. Black, A. Sorrentino, F. Fauth, I. Yousef, L. Simonelli, C. Frontera, A. Ponrouch, D. Tonti and M. R. Palacín, Synchrotron radiation based operando characterization of battery materials, *Chem. Sci.*, 2022, **14**, 1641–1665, DOI: **10.1039/d2sc04397a**.

39 M. Fehse, A. Iadecola, L. Simonelli, A. Longo and L. Stievano, The rise of X-ray spectroscopies for unveiling the functional mechanisms in batteries, *Phys. Chem. Chem. Phys.*, 2021, **23**, 23445–23465, DOI: **10.1039/d1cp03263a**.

40 S. Fazinić, M. Jakšić, L. Mandić and J. Dobrinić, Chemical dependence of second-order radiative contributions in the Kβ x-ray spectra of vanadium and its compounds, *Phys. Rev. A:At., Mol., Opt. Phys.*, 2006, **74**, 1–12, DOI: **10.1103/PhysRevA.74.062501**.

41 E. Gallo and P. Glatzel, Valence to core X-ray emission spectroscopy, *Adv. Mater.*, 2014, **26**, 7730–7746, DOI: **10.1002/adma.201304994**.

42 M. Rovezzi and P. Glatzel, Hard x-ray emission spectroscopy: A powerful tool for the characterization of magnetic

43 J. Rodríguez-Carvajal, Recent advances in magnetic structure determination by neutron powder diffraction, *Phys. B*, 1993, **192**, 55–69, DOI: **10.1016/0921-4526(93)90108-I**.

44 V. Briois, C. La Fontaine, S. Belin, L. Barthe, T. Moreno, V. Pinty, A. Carcy, R. Girardot and E. Fonda, ROCK: The new Quick-EXAFS beamline at SOLEIL, *J. Phys.:Conf. Ser.*, 2016, **712**, 012149, DOI: **10.1088/1742-6596/712/1/012149**.

45 B. Ravel and M. Newville, ATHENA and ARTEMIS: Interactive graphical data analysis using IFEFFIT, *Phys. Scr., T*, 2005, **T115**, 1007–1010, DOI: **10.1238/Physica.Topical.115a01007**.

46 C. J. Sahle, F. Gerbon, C. Henriquet, R. Verbeni, B. Detlefs, A. Longo, A. Mirone, M. C. Lagier, F. Otte, G. Spiekermann, S. Petitgirard and K. Kvashnina, A compact von Hámos spectrometer for parallel X-ray Raman scattering and X-ray emission spectroscopy at ID20 of the European Synchrotron Radiation Facility, *J. Synchrotron Radiat.*, 2023, **30**, 251–257, DOI: **10.1107/S1600577522011171**.

47 V. A. Solé, E. Papillon, M. Cotte, P. Walter and J. Susini, A multiplatform code for the analysis of energy-dispersive X-ray fluorescence spectra, *Spectrochim. Acta, Part B*, 2007, **62**, 63–68, DOI: **10.1016/j.sab.2006.12.002**.

48 J. J. H. Togonon, A. Iadecola, R. Wernert, K. Choudhary, M. Rovezzi, J.-N. Chotard, L. Stievano, A. Longo and L. Croguennec, Disentangling the ligand and electronic structure in KVPO4F1-xOx positive electrode materials by Valence-to-Core X-ray emission spectroscopy, *Energy Storage Mater.*, 2024, **69**, 103406, DOI: **10.1016/j.ensm.2024.103406**.

49 M. Guilmard, L. Croguennec and C. Delmas, Effects of Manganese Substitution for Nickel on the Structural and Electrochemical Properties of LiNiO[sub 2], *J. Electrochem. Soc.*, 2003, **150**, A1287, DOI: **10.1149/1.1601227**.

50 L. Croguennec, C. Pouillerie and C. Delmas, NiO[sub 2] Obtained by Electrochemical Lithium Deintercalation from Lithium Nickelate: Structural Modifications, *J. Electrochem. Soc.*, 2000, **147**, 1314, DOI: **10.1149/1.1393356**.

51 M. Mock, M. Bianchini, F. Fauth, K. Albe and S. Sicolo, Atomistic understanding of the LiNiO2-NiO2phase diagram from experimentally guided lattice models, *J. Mater. Chem. A*, 2021, **9**, 14928–14940, DOI: **10.1039/d1ta00563d**.

52 J. J. Rehr and A. L. Ankudinov, Progress in the theory and interpretation of XANES, *Coord. Chem. Rev.*, 2005, **249**, 131–140, DOI: **10.1016/j.ccr.2004.02.014**.

53 C. Delmas, M. Ménétrier, L. Croguennec, S. Levasseur, J. P. Peres, C. Pouillerie, G. Prado, L. Fournès and F. Weill, Lithium batteries: A new tool in solid state chemistry, *Int. J. Inorg. Mater.*, 1999, **1**, 11–19, DOI: **10.1016/S1463-0176(99)00003-4**.

54 N. Ikeda, I. Konuma, H. B. Rajendra, T. Aida and N. Yabuuchi, Why is the O3 to O1 phase transition hindered in LiNiO2on full delithiation?, *J. Mater. Chem. A*, 2021, **9**, 15963–15967, DOI: **10.1039/d1ta03066c**.

semiconductors, *Semicond. Sci. Technol.*, 2014, **29**, 023002, DOI: **10.1088/0268-1242/29/2/023002**.

55 S. D. Gamblin and D. S. Urch, Metal Kβ X-ray emission spectra of first row transition metal compounds, *J. Electron Spectrosc. Relat. Phenom.*, 2001, **113**, 179–192, DOI: **10.1016/S0368-2048(00)00416-3**.

56 J. J. H. Togonon, A. Longo, R. Wernert, L. Stievano, M. Rovezzi, J.-N. Chotard, A. Iadecola and L. Croguennec, Probing the structural and electronic heterogeneity of LiVPO4F and KVPO4F positive electrode materials by combined X-ray absorption and emission spectroscopy, *Mater. Today Chem.*, 2025, **44**, 102541, DOI: **10.1016/j.mtchem.2025.102541**.

57 C. J. Pollock, M. U. Delgado-Jaime, M. Atanasov, F. Neese and S. Debeer, Kβ mainline X-ray emission spectroscopy as an experimental probe of metal-ligand covalency, *J. Am. Chem. Soc.*, 2014, **136**, 9453–9463, DOI: **10.1021/ja504182n**.

58 S. Lafuerza, A. Carlantuono, M. Retegan and P. Glatzel, Chemical Sensitivity of Kβ and Kα X-ray Emission from a Systematic Investigation of Iron Compounds, *Inorg. Chem.*, 2020, **59**, 12518–12535, DOI: **10.1021/acs.inorgchem.0c01620**.

59 J. P. Rueff, V. Baledent, K. Higashi and H. Kageyama, Spin transition in SrFeO2 under pressure by x-ray spectroscopy, *Phys. Rev. B*, 2020, **102**, 1–5, DOI: **10.1103/PhysRevB.102.235138**.

60 U. Bergmann, C. R. Horne, T. J. Collins, J. M. Workman and S. P. Cramer, Chemical dependence of interatomic X-ray transition energies and intensities - a study of Mn Kβ'' and Kβ2, 5 spectra, Chem, *Phys. Lett.*, 1999, **302**, 119–124, DOI: **10.1016/S0009-2614(99)00095-0**.

61 S. Fazinić, L. Mandić, M. Kavčič and I. Božičević, Parametrization of Kβ'' and Kβ2,5 X-ray contributions in Kβ spectra of 3d transition metal compounds, *J. Anal. At. Spectrom.*, 2011, **26**, 2467–2476, DOI: **10.1039/c1ja10176e**.

62 F. Lin, D. Nordlund, I. M. Markus, T. C. Weng, H. L. Xin and M. M. Doeff, Profiling the nanoscale gradient in stoichiometric layered cathode particles for lithium-ion batteries, *Energy Environ. Sci.*, 2014, **7**, 3077–3085, DOI: **10.1039/c4ee01400f**.

63 H. Wang, D. S. Patil, W. Gu, L. Jacquamet, S. Friedrich, T. Funk and S. P. Cramer, L-edge X-ray absorption spectroscopy of some Ni enzymes: Probe of Ni electronic structure, *J. Electron Spectrosc. Relat. Phenom.*, 2001, **114–116**, 855–863, DOI: **10.1016/S0368-2048(00)00370-4**.

64 A. N. Mansour and C. A. Melendres, Analysis of X-ray absorption spectra of some nickel oxycompounds using theoretical standards, *J. Phys. Chem. A*, 1998, **102**, 65–81, DOI: **10.1021/jp9619853**.

65 F. De Groot, G. Vankó and P. Glatzel, The 1s x-ray absorption pre-edge structures in transition metal oxides, *J. Phys.:Condens. Matter*, 2009, **21**(10), 104207, DOI: **10.1088/0953-8984/21/10/104207**.

66 F. Frati, M. O. J. Y. Hunault and F. M. F. De Groot, Oxygen K-edge X-ray Absorption Spectra, *Chem. Rev.*, 2020, **120**, 4056–4110, DOI: **10.1021/acs.chemrev.9b00439**.

67 A. Grimaud, W. T. Hong, Y. Shao-Horn and J.-M. Tarascon, Anionic redox processes for electrochemical devices, *Nat. Mater.*, 2016, **15**, 121–126, DOI: **10.1038/nmat4551**.

68 B. Li, M. T. Sougrati, G. Rousse, A. V. Morozov, R. Dedryvère, A. Iadecola, A. Senyshyn, L. Zhang, A. M. Abakumov, M. L. Doublet and J.-M. Tarascon, Correlating ligand-to-metal charge transfer with voltage hysteresis in a Li-rich rock-salt compound exhibiting anionic redox, *Nat. Chem.*, 2021, **13**, 1070–1080, DOI: **10.1038/s41557-021-00775-2**.

69 Q. Jacquet, A. Iadecola, M. Saubanère, H. Li, E. J. Berg, G. Rousse, J. Cabana, M. L. Doublet and J.-M. Tarascon, Charge Transfer Band Gap as an Indicator of Hysteresis in Li-Disordered Rock Salt Cathodes for Li-Ion Batteries, *J. Am. Chem. Soc.*, 2019, **141**, 11452–11464, DOI: **10.1021/jacs.8b11413**.

70 D. Asakura, T. Sudayama, Y. Nanba, E. Hosono, H. Kiuchi, K. Yamazoe, J. Miyawaki, Y. Harada, A. Yamada, R.-P. Wang and F. M. F. de Groot, Elucidation of the Co 4+ state with strong charge-transfer effects in charged LiCoO2 by resonant soft X-ray emission spectroscopy at the Co L3 edge, *Phys. Chem. Chem. Phys.*, 2025, **27**(8), 4092, DOI: **10.1039/D4CP03759F**.

71 H. Banerjee, M. Aichhorn, C. P. Grey and A. J. Morris, Insulating behaviour in room temperature rhombohedral LiNiO 2 cathodes is driven by dynamic correlation, *JPhys Energy*, 2024, **6**, 045003, DOI: **10.1088/2515-7655/ad7980**.

72 P. Kuiper, G. Kruizinga, J. Ghijsen, G. A. Sawatzky and H. Verweij, Character of Holes in LixNi1−xO and Their Magnetic Behavior, *Phys. Rev. Lett.*, 1989, **62**, 1214, DOI: **10.1103/physrevlett.62.1214**.